

Realizing Rapid, High-Fidelity, Single-Shot Dispersive Readout of Superconducting Qubits

T. Walter,* P. Kurpiers,* S. Gasparinetti, P. Magnard, A. Potočnik,
Y. Salathé, M. Pechal, M. Mondal, M. Oppliger, C. Eichler, and A. Wallraff
Department of Physics, ETH Zurich, CH-8093 Zurich, Switzerland

(Dated: January 26, 2017)

The speed of quantum gates and measurements is a decisive factor for the overall fidelity of quantum protocols when performed on physical qubits with finite coherence time. Reducing the time required to distinguish qubit states with high fidelity is therefore a critical goal in quantum information science. The state-of-the-art readout of superconducting qubits is based on the dispersive interaction with a readout resonator. Here, we bring this technique to its current limit and demonstrate how the careful design of system parameters leads to fast and high-fidelity measurements without affecting qubit coherence. We achieve this result by increasing the dispersive interaction strength, by choosing an optimal linewidth of the readout resonator, by employing a Purcell filter, and by utilizing phase-sensitive parametric amplification. In our experiment, we measure 98.25% readout fidelity in only 48 ns, when minimizing read-out time, and 99.2% in 88 ns, when maximizing the fidelity, limited predominantly by the qubit lifetime of 7.6 μ s. The presented scheme is also expected to be suitable for integration into a multiplexed readout architecture.

I. INTRODUCTION

High fidelity single-shot qubit readout is quintessential for realtime quantum feedback schemes used for example in error correction [1, 2], teleportation [3, 4], and state initialization [5, 6]. It is also a key element in fundamental tests of quantum mechanics, such as loophole-free Bell tests [7–9]. Experimental progress in these areas may ultimately lead to fault-tolerant quantum computation, for which, one of the most promising platforms is built on superconducting circuits and qubits. The standard technique to probe these qubits relies on the state-dependent dispersive frequency shift imposed by the qubit on a coupled resonator [10, 11]. While averaging was required early on to determine the qubit state [11], advances in quantum limited amplification [12–15] allowed for the observation of quantum jumps and the discrimination of qubit states in single shot measurements [16, 17]. In an attempt to further improve readout fidelities and measure multiple qubits simultaneously, Purcell filters [18–20] and broadband parametric amplifiers were developed [21–23]. With these advances, state discrimination is now predominantly limited by qubit decay during the time of measurement [22, 24, 25].

In order to overcome this limitation, one can reduce the measurement time, which we achieve in this work by increasing the dispersive interaction strength and by choosing an appropriate resonator linewidth. In addition, we use a Purcell filter to protect the qubit from radiative decay, and efficiently detect the microwave fields with a quantum limited phase-sensitive amplifier. In our readout experiments we discriminate between the qubit ground and excited state with a fidelity in excess of 98% in less than 50 ns. Further, we show that the measure-

ment time can be reduced by using a shaped “two-step” readout pulse that populates the resonator faster with microwave photons than a simple square pulse [19, 26].

II. DISCUSSION OF THE EXPERIMENT

Our sample device, depicted in Fig. 1(a), consists of a transmon qubit (purple) coupled capacitively with rate $g/2\pi = 208$ MHz to a readout resonator (green). The qubit, which is fabricated from shadow evaporated aluminum, has a transition frequency of $\omega_q/2\pi = 6.316$ GHz, an anharmonicity of $\alpha/2\pi = -340$ MHz and a lifetime $T_1 = 7.6$ μ s. The qubit state is controlled by applying microwave pulses through a capacitively coupled drive line (teal). The readout resonator, together with the remaining on-chip elements, is fabricated from a niobium thin film sputtered on a sapphire substrate using photolithography and reactive ion etching. The readout resonator has a center frequency of $\omega_r/2\pi = 4.754$ GHz. The detuning $\Delta = \omega_q - \omega_r$ is much larger than g , which results in a dispersive coupling between qubit and resonator with rate $\chi/2\pi = -7.9$ MHz. The resonator is coupled through a Purcell filter cavity [19, 27] to an external measurement line (orange structure in Fig. 1a). The effective resonator linewidth $\kappa_{\text{eff}} = 4Q_p J^2 / (\omega_p + 4\delta_p^2 Q_p^2 / \omega_p)$ is controlled by the coupling strength $J/2\pi = 25$ MHz between readout resonator and Purcell filter and the detuning $\delta_p/2\pi = 2$ MHz between the two. With the quality factor of the Purcell filter cavity $Q_p = 74$ we find $\kappa_{\text{eff}}/2\pi = 37.5$ MHz.

The sample is probed in a dilution refrigerator at a temperature of 10 mK using a standard microwave frequency measurement setup (Fig. 5a). A Josephson Parametric Dimer (JPD) amplifier [28] operated in the phase-sensitive mode is used to optimize the measurement efficiency to achieve $\eta = 0.66$, with a 3 dB bandwidth of 27 MHz and a gain of 26 dB [13, 15], see Appendix C for

* These authors contributed equally to this work

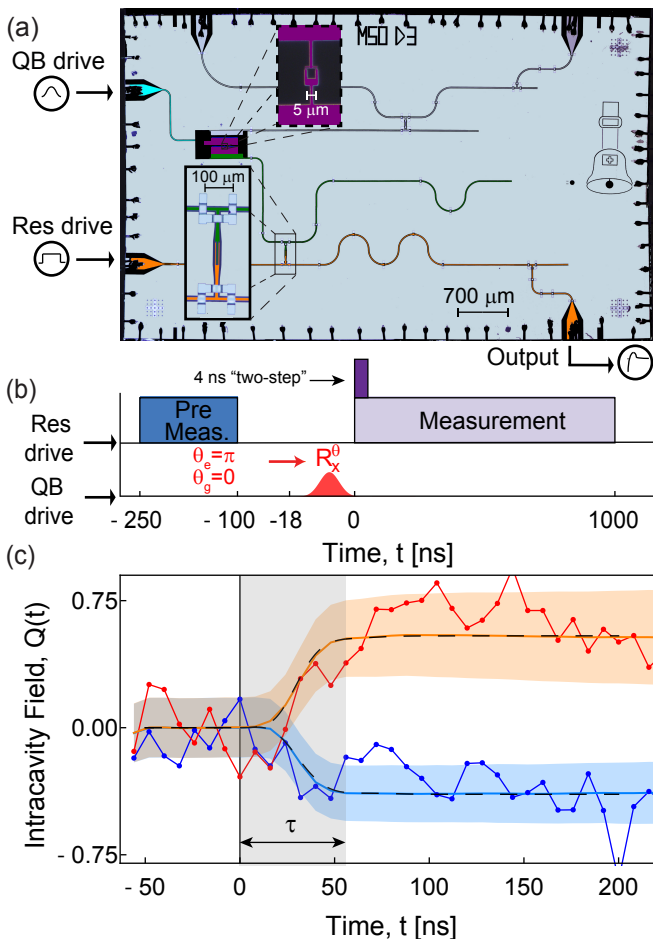


FIG. 1. (a) False color micrograph of the experimental sample (see text for details). (b) Pulse scheme including the preselection procedure, the “gated” (light purple) and the “two-step” measurement pulse (dark+light purple), see text for details. (c) A characteristic ground (blue) and excited (red) single-shot trajectory plotted together with the mean of all ground and excited trajectories (light blue/ light red solid lines) with their respective standard deviations (blue and orange shaded regions). The black dashed line shows the theoretically expected dynamics. The gray region depicts the typical integration time τ of the experiment.

details.

To read out the qubit, we apply a coherent tone at $t = 0$ to the input port of the Purcell filter (orange in Fig. 1(a)) at the center frequency $\omega_d = \omega_r$ between the two state-dependent resonator frequencies. The power is chosen to maximize the readout fidelity and corresponds to $n_{\text{drive}} = 2.5 \pm 0.25$ photons in the readout resonator, which we have calibrated based on an ac-Stark shift measurement, see Appendix A. At $t = -250$ ns we apply a 150 ns long measurement pulse to the device, see pulse sequence in Fig. 1(b). We use the last 50 ns of this pulse to determine the state of the qubit and later analyze only those traces for which the qubit is found in the ground state. This procedure we refer to as preselection (Appendix B). Before preparing the qubit in

either the ground or excited state by applying a 18 ns R_x^π DRAG pulse [29, 30], which ends at $t = 0$, we wait for about 100 ns $\approx 25/\kappa_{\text{eff}}$ for the resonator to decay back to its vacuum state after preselection. In addition to the typical square (“gated”) measurement pulse generated by gating the signal source, we also utilize a “two-step” pulse, which has an additional 4 ns high power segment that drives the resonator into its steady state more rapidly [19, 26], see pulse sequence in Fig. 1(b).

A field-programmable gate array (FPGA) with an analog-to-digital converter (ADC) samples the output signal in 8 ns time bins. The amplified quadrature of the JPD is chosen to maximize the contrast between the mean ground and excited state response in a single quadrature $Q(t)$. As shown in Fig. 1(c), the ground and excited state response can be clearly distinguished in a single shot of a measurement. With the qubit prepared in the excited state, due to qubit relaxation, the averaged response $\langle Q_e(t) \rangle$ (solid orange line) slightly decays towards the ground state response $\langle Q_g(t) \rangle$, resulting in the corresponding standard deviation $\langle \Delta Q_e(t) \rangle$ (shaded orange region) to grow in time. These trends limit the distinguishability between ground and excited state and highlight the need for fast readout.

The theoretical dynamics of the Purcell filter [27] (dashed black lines), including the analog and digital filtering of the measurement line (see Section III and Appendix D), show very good agreement with the averaged trajectories and allows us to calibrate the starting time of the measurement. We chose $t = 0$ to be the time at which the square readout pulse arrives at the input of the Purcell filter.

In order to optimize the distinguishability between the ground and excited state, given a certain integration time τ , we evaluate the integrated readout quadrature value $q_\tau = \sqrt{\kappa_p} \int_0^\tau dt Q(t) W(t)$, where the weighting function $W(t) \propto |Q_e(t) - Q_g(t)|$ is proportional to the average difference between the ground and excited state responses and is normalized to $\int_0^\tau dt W^2(t) = 1$.

We perform 60,000 repetitions of the experiment, alternating the qubit preparation between ground and excited state, and populate histograms of q_τ , as shown in Fig. 2. The ground and excited state histograms are simultaneously fit to the sum of two Gaussians, as described in Appendix B. From these fits we extract a decision boundary, or threshold q_τ^{th} , at the intersection point of the two fitted state distributions. The measurement is then characterized by its fidelity, defined as [31]

$$F = 1 - P(e|g) - P(g|e) \quad (1)$$

where $P(x|y)$ is the probability that the qubit prepared in state y is measured to be in state x . The fidelity is extracted directly from the experimental data as 1 minus the sum of the fraction of ground state preparation events with $q_\tau \geq q_\tau^{\text{th}}$, and the fraction of excited state preparation events with $q_\tau < q_\tau^{\text{th}}$, denoted ϵ_g and ϵ_e respectively.

At short measurement times $\tau \lesssim 40$ ns, as shown in

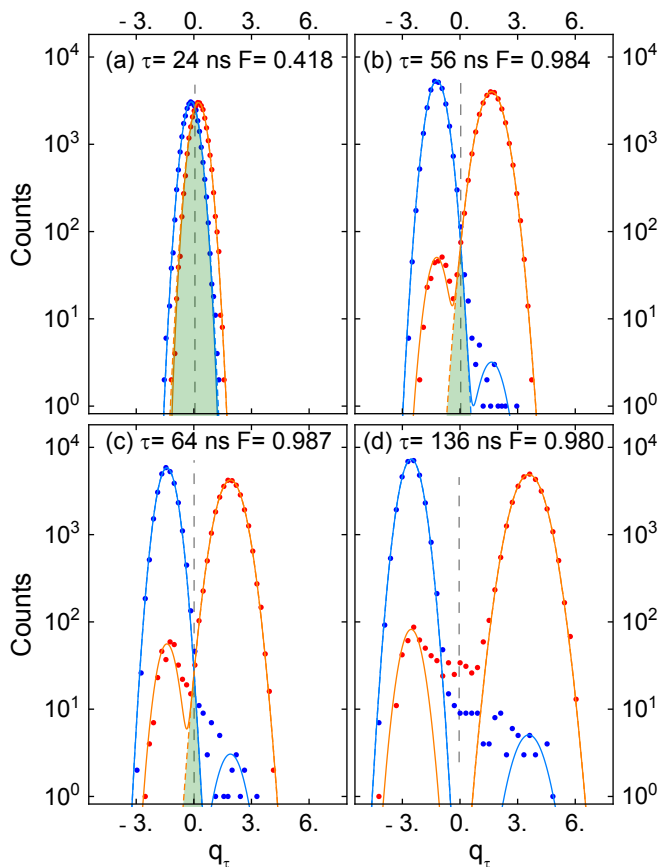


FIG. 2. Histograms of the integrated quadrature amplitude q_τ at selected integration times between 24 and 136 ns (a-d) after preparing the qubit in the ground (blue) or excited (red) state. The single shots were performed with a gated measurement pulse and optimal drive power. The solid lines are fits to a double Gaussian model whose individual components are indicated as dashed lines. The green areas depict the overlap error. The dashed gray line indicates the qubit state threshold.

Fig. 2(a), the mean state trajectories have yet to reach their maximum separation, leaving a large overlap of the two distributions (green area). However, at longer integration times the separation grows sufficiently compared to the standard deviations, allowing us to clearly resolve the two states. With continued integration the uncertainties further reduce, reaching a maximal distinguishability at $\tau = 64$ ns, see Fig. 2(c). For even longer integration times, transitions between the two states during the measurement, due to spontaneous emission, thermal excitation or transitions induced by the readout tone, limit the fidelity.

We further analyze the data by separating the overlap error from transition errors. The overlap error ϵ_o between the two state distributions is defined as the normalized green area indicated in Fig. 2 and is a measure for how distinguishable the two distributions are [19, 31]. It can be further decomposed into contributions from the ground and excited state $\epsilon_o = \epsilon_{o,g} + \epsilon_{o,e}$. The remaining

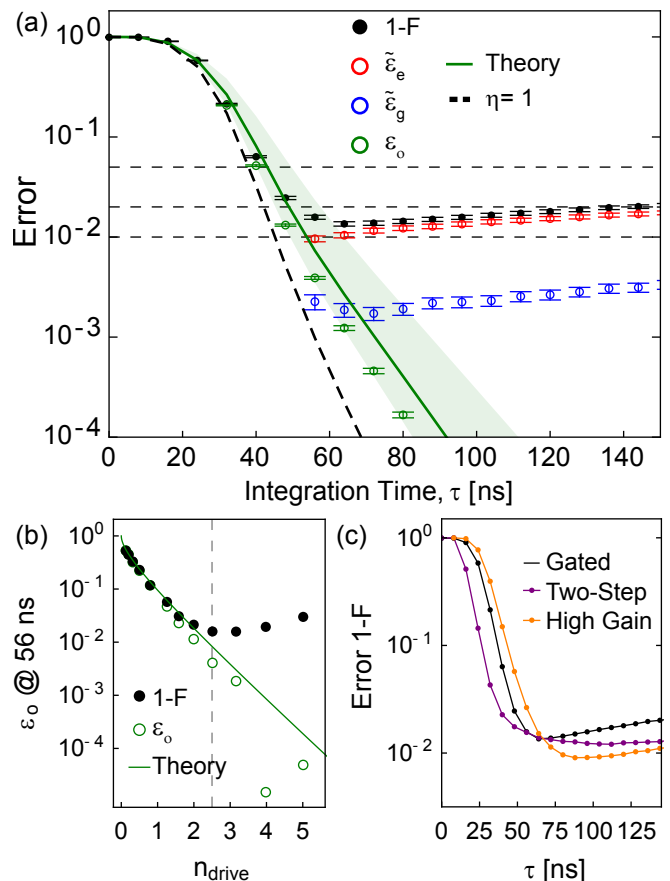


FIG. 3. (a) Errors ϵ of the gated single-shot experiment at optimal drive strength $n_{\text{drive}} = 2.5$ as a function of integration time τ . The solid black circles represent the infidelity extracted from the data directly. The open circles are excited (red) ground state (blue) and overlap errors (green) extracted from the fits. The solid green line is the numerical solution of the full model for the overlap error (Eq. D1) with the independently measured system parameters including the finite amplifier bandwidth, while the black dashed curve assumes $\eta = 1$. (b) Results of the overlap error ϵ_o at 56 ns extracted from Gaussian fits (green circles) with the gated single-shot experiments versus measurement drive power n_{drive} . The green solid line is the theoretical prediction using the full overlap model (Eq. D1), while the black dots are the measured infidelity $1 - F$. (c) Experimental results of infidelity versus integration time for the gated (black), two-step (purple) and high amplifier gain (orange) measurements.

transition errors $\tilde{\epsilon}_x = \epsilon_x - \epsilon_{o,x}$, where x is the state of the qubit, are due to failed preparation events and transitions during the measurement. The transition errors are found to be larger for a prepared excited state and increase with τ proportional to $1 - e^{-\tau/T_1}$ due to spontaneous emission. The overlap errors $\epsilon_{o,x}$ decrease with integration time, see Fig. 3.

For $\tau = 56$ ns we obtain a fidelity of $98.42 \pm 0.07\%$ and an overlap error of $\epsilon_o = 0.39 \pm .01\%$, equal to that reported in Ref. [19], but achieved in roughly a third of the integration time. We also have an average assignment

fidelity of 99.2%, higher than that reported in Ref. [32], while using less than a fourth of the integration time. We also achieve this higher fidelity with a qubit lifetime of 70% and 30% of those in the two references [19, 32], respectively. This further emphasizes the effectiveness of fast, optimized readout. At this integration time, the normalized ground state error $\tilde{\epsilon}_g = 0.23 \pm 0.04\%$ and normalized excited state error is $\tilde{\epsilon}_e = 0.96 \pm 0.06\%$. The limited qubit lifetime $T_1 = 7.6 \mu\text{s}$ accounts for 76% of the excited state error. We attribute the remaining part to measurement induced mixing [33]. This hypothesis is supported by its equivalence to the ground state error and the low thermal occupation of the qubit (see Appendix B). This mixing error is a consequence of driving the system stronger in order to reduce the overlap faster and reach a higher fidelity in a shorter time. However, some errors may be introduced by imperfect state preparation and therefore this estimate for the measurement induced mixing is an upper-bound.

We also performed the gated measurements at different drive strengths and found the overlap error decreases monotonically with the measurement power, Fig. 3(b). This behavior is in good agreement with theory [31] (Appendix D). However, the overall error of the readout protocol reaches a minimum at $n_{\text{drive}} = 2.5$ before rising again due to measurement induced mixing.

To further improve the readout speed at the optimal power, we repeated the experiment with the two-step pulse shape introduced earlier [19, 26], which more rapidly drives the resonator to its steady-state. The readout fidelity during the rise time of the signal was consistently 8 ns faster than in the gated measurements, as shown in Fig. 3(c), and reaches a nearly identical fidelity of $F = 98.25 \pm .05\%$ in only 48 ns.

We also studied the dependence of readout fidelity on the measurement efficiency η by increasing the gain of the JPD to 35 dB. This caused a reduction of the amplifier bandwidth to 10 MHz, but increased the efficiency to $\eta = 0.75$ (see Appendix C). In this configuration we measured the highest fidelity at 99.2%, however, the integration time of 88 ns required to achieve this fidelity is longer due to the reduced bandwidth, see orange line in Fig. 3(c).

III. MODEL USED FOR OPTIMIZING THE READOUT

A. Dynamics of readout circuit

For phase-sensitive amplification the information acquired about the qubit state is proportional to the difference between the ground and excited state response in one quadrature $S(t) = \sqrt{\kappa_p} |Q_e(t) - Q_g(t)|$ where κ_p is the linewidth of the Purcell filter [27]. This is approximately equal to $S(t) \approx \sqrt{\kappa_p} |\beta_e(t) - \beta_g(t)|$ were, $\beta_{g,e}$ are the complex intracavity field amplitudes of the Purcell filter when the qubit is in the ground or excited state. In the quasisteady state limit (QSS) given

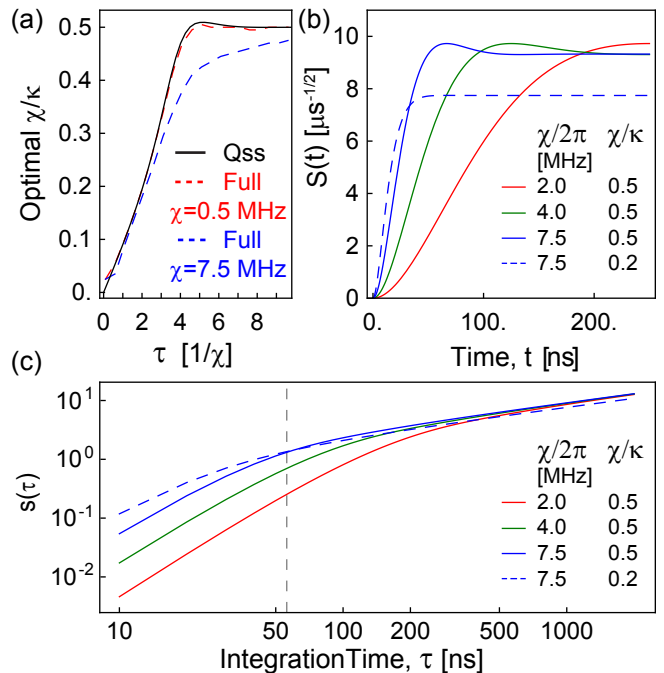


FIG. 4. (a) Ratio χ/κ that maximizes $s(\tau)$ as a function of integration time τ . The solid black line represents the quasisteady state solution, while the dashed lines are the numerical solutions with our circuit parameters with the full model [27] which includes the dynamics of the Purcell filter. (b) Measurement signal $S(t)$ as a function of time t for the indicated values of χ . The solid lines indicate a ratio $\chi/\kappa = 0.5$, while the dashed line is for our experimentally used ratio of 0.2, chosen for being optimal for short integration times below 50 ns. (c) Integrated signal $s(\tau)$ as a function of integration time τ , for the indicated values of χ and χ/κ . The gray dashed line represents the typical integration time used in our experiment. For both $S(t)$ and $s(\tau)$ we have used $\alpha/2\pi = -340$ MHz, $\Delta/2\pi = 1562$ MHz, and $n_{\text{drive}} = n_{\text{crit}}/5$.

by $J \ll \kappa_p$, the full system dynamics can be reduced to the dynamics of the readout resonator, such that $S(t) \approx \sqrt{\kappa_{\text{eff}}} |\alpha_e(t) - \alpha_g(t)|$, where $\alpha_{e,g}$ are the complex intracavity field amplitudes of the readout resonator. By considering $\omega_d = \omega_r = \omega_p$, for a gated measurement pulse, we find an analytical solution for

$$S(t) \approx \sqrt{\frac{n_{\text{drive}}}{n_{\text{crit}}}} \left| \frac{\alpha}{(1 + \alpha/\Delta)} \right| \frac{1}{|\chi/\kappa_{\text{eff}}| (1 + (2\chi/\kappa_{\text{eff}})^2)} \left(2 \left| \frac{\chi}{\kappa_{\text{eff}}} \right| + e^{-\pi\kappa_{\text{eff}}t} \sin(2\pi\chi t) - 2e^{-\pi\kappa_{\text{eff}}t} \cos(2\pi\chi t) \right) \quad (2)$$

where χ is

$$\chi = \frac{g^2}{\Delta} \frac{\alpha}{(\Delta + \alpha)} = \frac{\alpha}{4n_{\text{crit}}} \frac{1}{(1 + \frac{\alpha}{\Delta})} \quad (3)$$

and $n_{\text{crit}} = \Delta^2/4g^2$ is the readout resonator's critical photon number [10].

The readout fidelity after a measurement time τ is directly related to the integrated information rate $s(\tau) = (1/\sqrt{\tau}) \int S(t) dt$ (see Eq. D1). In the following, we therefore study $s(\tau)$ and optimize it with respect to the accessible system parameters.

We first consider the influence of the effective linewidth κ_{eff} at otherwise constant parameters α , $n_{\text{drive}}/n_{\text{crit}}$, Δ and χ . For integration times well into steady state we find $s(\tau)$ to be maximized for $|\chi/\kappa_{\text{eff}}| = 0.5$ independent of all other parameters [31], see Fig. 4(a). However, at integration times $\chi\tau \lesssim 4.5$ one could achieve a higher fidelity by increasing κ_{eff} with respect to χ . This increases $S(t)$ at short times while reducing its steady state value. We note that, this initial speed up could also be achieved by using a two-step pulse while maintaining $\chi/\kappa = 0.5$ independent of the integration time.

When χ and therefore κ_{eff} becomes comparable to κ_{p} , one must solve the complete system dynamics beyond the QSS solution including the dynamics of the Purcell-filter [27]. We have plotted the full solution with the experimentally realized system parameters as the blue dashed line in Fig. 4(a) which shows a slower convergence to the steady state ratio than the QSS solution.

For the optimal ratio $\chi/\kappa_{\text{eff}} = 0.5$, we also see from Fig. 4(a) that the time required to reach steady state is inversely proportional to χ . This emphasizes that in order to achieve fast readout a large χ is favorable. Therefore, if one can maintain the optimal ratio, then larger χ will more rapidly accumulate signal. By successfully realizing these concepts in the experiment, we were able to achieve a higher single-shot fidelity at shorter integration times than previously reported, where it is less affected by qubit relaxation time T_1 . We chose the ratio $|\chi/\kappa_{\text{eff}}| = 0.2$ in our experiment to optimize for an integration time of 50 ns or less using the gated measurement pulse. This is illustrated in Fig. 4(b-c) where the integrated signal is larger for $|\chi/\kappa_{\text{eff}}| = 0.2$ than for $|\chi/\kappa_{\text{eff}}| = 0.5$ for $\tau < 50$ ns.

B. Constraints

The optimal set of parameters are typically subject to experimental constraints of the system. With the use of Purcell filters [18-20], $|\chi/\kappa_{\text{eff}}| \approx 1/2$ can be maintained for larger values of χ , without reaching a Purcell limited qubit lifetime [34]. In this case, the limitation for readout speed derives directly from the upper bound of χ .

For larger χ , a large anharmonicity is advantageous, see Eq. 3. However with the use of a transmon qubit, large α reduces the qubit's coherence time through charge dispersion [35]. Charge dispersion scales exponentially with the ratio of the Josephson energy to the charging energy, E_J/E_C [34] and therefore with the qubit frequency and anharmonicity. For our sample, we chose an anharmonicity which results in an estimated upper-bound for the dephasing time of 150 μs with a qubit near 6.3 GHz. Our sample, however, did not realize this upper-bound

due to other dephasing mechanisms and fabrication limitations.

The second constraint on χ derives from its inverse relationship to the critical photon number $n_{\text{crit}} \propto 1/\chi$ (Eq. 3). The dispersive approximation remains valid only in the limit $n_{\text{crit}} \gg 1$, leading to an upper bound on χ . Furthermore, n_{crit} limits the number of photons that can be used for readout without driving unwanted qubit transitions. The probability for such a transition is proportional to the parameter [10, 36]

$$\lambda = \sin^2 \left(\frac{1}{2} \tan^{-1} \left(\sqrt{\frac{n_{\text{drive}} + 1}{n_{\text{crit}}}} \right) \right) \quad (4)$$

implying the constraint $n_{\text{drive}} \ll n_{\text{crit}}$. As a suitable trade off between these limitations, we chose $n_{\text{crit}} \approx 13$ and $n_{\text{drive}} \approx n_{\text{crit}}/5$, resulting in $\lambda \sim 1.8\%$. In our experiment, this leads to a measurement induced error $< 0.23\%$ at $\tau = 56$ ns.

Additionally, the mixing rates of the qubit states during measurement may also depend on higher order transmon states [37, 38], as well as, the power spectrum of the flux noise $\Gamma_{\uparrow\downarrow} \propto (n_{\text{drive}}/n_{\text{crit}}) N_f(\pm\Delta)$, where N_f is the flux noise power at detuning $\pm\Delta$ [39]. Slichter et. al. [40] measured a $N_f \propto 1/f$ flux noise dependency and therefore we designed a $g/2\pi \approx 210$ MHz to keep the detuning $\Delta/2\pi \approx 1.6$ GHz sufficiently large for our chosen n_{crit} . We further utilized a positive detuning Δ to exploit the asymmetry in χ with respect to Δ which allows for a large $\chi/2\pi > -7.5$ MHz and remain within these constraints.

IV. CONCLUSIONS

In summary, we have demonstrated an increase in speed and fidelity of qubit readout by optimizing the circuit parameters. Further, we have identified constraints on χ imposed by the nature of the transmon qubit and its dispersive interaction. The limits to the qubit lifetime and dephasing time imposed by our choice of circuit parameters is expected to be 600 μs and 150 μs respectively, while other mechanisms not considered may impose shorter times. We therefore believe our design concepts are extensible to a multiplexed readout architecture [41].

While improvements in the qubit T_1 and in the amplifier performance are at this point well understood to further improve the readout, the role of measurement induced mixing as a limiting factor remains an aspect worth further investigation.

ACKNOWLEDGEMENTS

The authors would like to thank J. Heinsoo for his efforts on improving our automated qubit calibration software which helps characterize our qubits and optimize

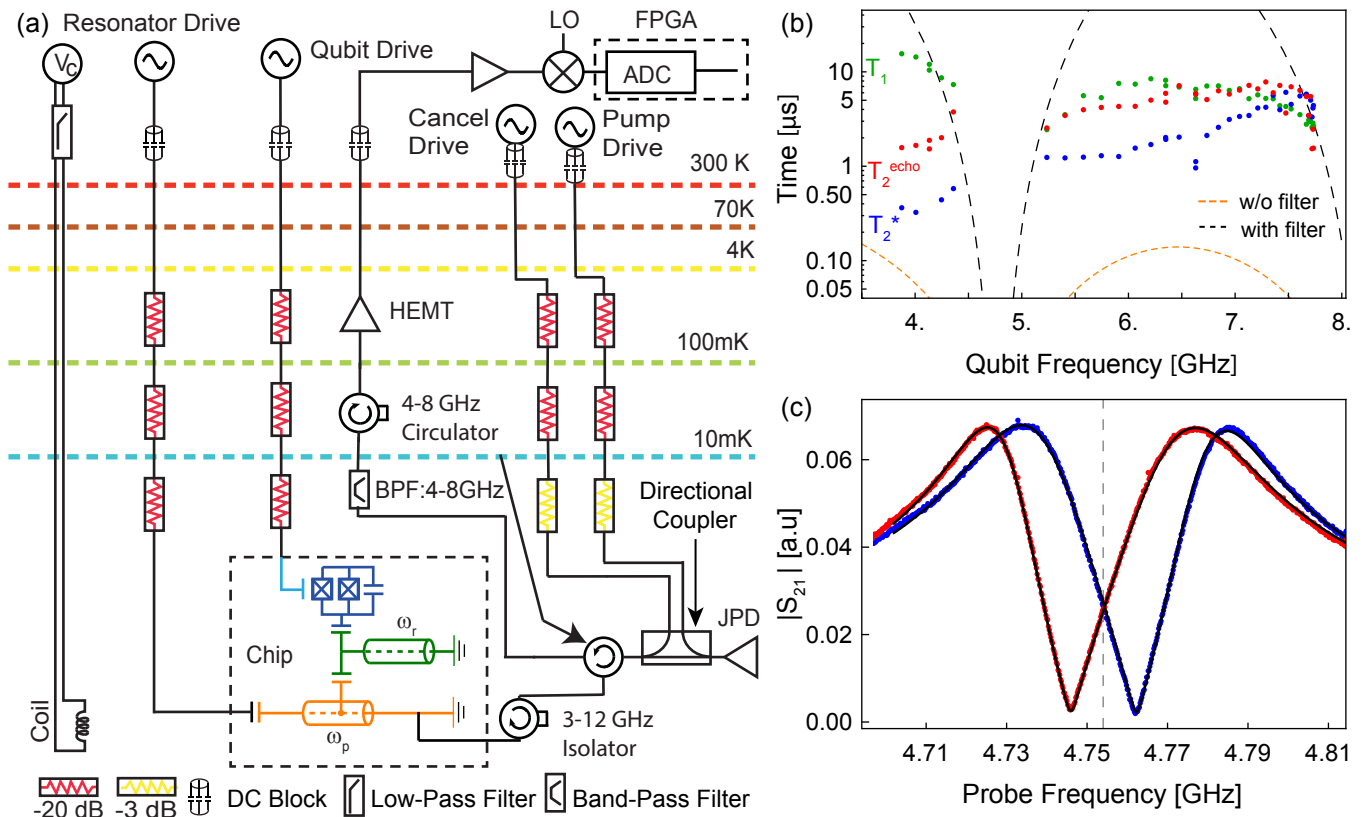


FIG. 5. (a) Schematic of the experimental setup. (b) Measured lifetime T_1 , Ramsey decay time T_2^* , and spin echo time T_2^{echo} as a function of the qubit frequency. The black and orange dashed lines are the theoretical Purcell lifetimes with and without the band pass filter. (c) Measured transmission of readout line with the qubit in its ground (blue) and excited (red) state. The solid black lines are fits to the input-output model of the circuit used to extract the relevant parameters of the system.

the control gates. Additionally, we thank M. Collodo, C. K. Andersen, S. Krinner, L. Govia and A. Clerk for discussions.

This work is supported by the European Research Council (ERC) through the ‘‘Superconducting Quantum Networks’’ (SuperQuNet) project, by National Centre of Competence in Research ‘‘Quantum Science and Technology’’ (NCCR QSIT), a research instrument of the Swiss National Science Foundation (SNSF), by the Office of the Director of National Intelligence (ODNI), Intelligence Advanced Research Projects Activity (IARPA), via the U.S. Army Research Office grant W911NF-16-1-0071 and by ETH Zurich. The views and conclusions contained herein are those of the authors and should not be interpreted as necessarily representing the official policies or endorsements, either expressed or implied, of the ODNI, IARPA, or the U.S. Government. The U.S. Government is authorized to reproduce and distribute reprints for Governmental purposes notwithstanding any copyright annotation thereon.

Appendix A: Setup details and sample characterization

In this section we describe the measurement setup, discuss basic sample characterization measurements and the ac-Stark shift calibration of the readout power.

A measurement signal applied to the sample exits the output port of the band pass Purcell filter of the sample and passes through an isolator, a circulator and a directional coupler before entering the Josephson Parametric Dimer (JPD), see Fig. 5(a). The signal then passes through additional amplification stages before it is down converted to 250 MHz and finally is digitized at the ADC connected to the FPGA. The ADC samples the signal at a 1 GHz rate. Within the FPGA the signal is digitally down-converted to DC and integrated for 8 ns in order to remove the down converted low frequency noise and LO leakage from the analog down conversion process. The result of the FPGA calculations are then stored for the analysis discussed in the main text.

The implementation of a band pass Purcell filter improves the lifetime of our qubit beyond the limit imposed by the readout resonator bandwidth through the Purcell effect [42], shown in Fig. 5(b). The measured lifetime

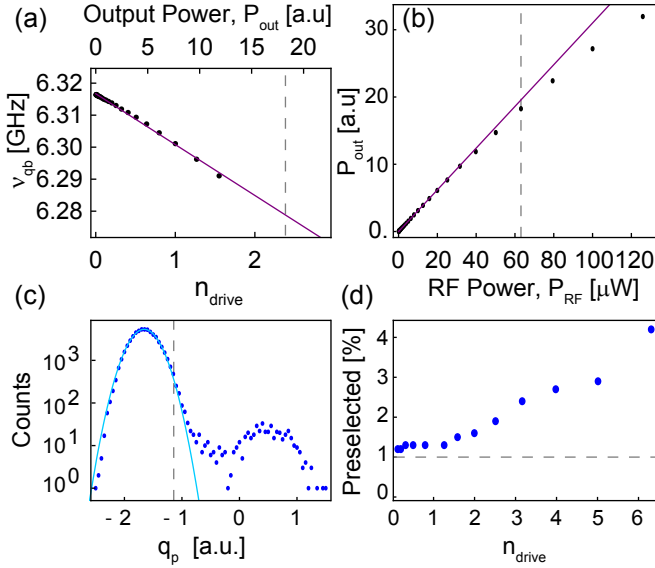


FIG. 6. (a) Qubit frequency ν_{qb} (black dots) as a function of measured power P_{out} with a linear fit (purple line). The calibrated photon number is shown on the bottom axis and the gray dashed line indicates the optimal drive power used in the experiment. (b) Measured output power as a function of input power P_{RF} . The purple line is a linear fit to the low power data while the gray dashed line indicates the optimal drive power. (c) Mean value q_p of the last 50 ns of the preselection pulse (blue points) for $n_{drive} = 2.5$ with Gaussian fit (light blue line) and the state discrimination threshold (dashed vertical line) is set to the 99% of the fitted cumulative distribution function. This guarantees that the majority of thermally excited states identified by integrated measurement values larger than the threshold are rejected. (d) Percentage of removed data after preselection analysis as a function of drive power. The gray dashed line indicates the minimum percent of traces which could be removed due to our choice of the preselection state discrimination threshold.

(green dots) is between 30 and 100 times longer than the T_1 times predicted without the Purcell filter (orange dashed line). However, it is often shorter than the limit imposed by the Purcell filter (black dashed line) which we attribute to limitations in our fabrication techniques. The dephasing time of this qubit was $2T_1 \approx 5 \mu s$ at the maximum qubit frequency (T_1 is Purcell limited here), where the sensitivity to flux noise is minimized, and then decreases compared to T_1 when the qubit is tuned to lower frequencies.

We characterize the sample by performing resonator spectroscopy. We plot the transmission through the Purcell filter as a function of probe frequency for the ground (blue) and excited (red) qubit states in Fig. 5(c). From these transmission spectra, the values of ω_p , ω_r , J , χ , and $Q_p = \omega_p/\kappa_p$ are extracted from the fit parameters of the input-output model of the circuit given by

$$|S_{21}|_{\pm} \propto \frac{\kappa_p}{\frac{(\gamma + \kappa_p)}{2} + i(\omega_p - \omega) + \frac{2J^2}{\gamma + 2i(\omega_r \pm \chi - \omega)}} \quad (A1)$$

where γ is the small internal loss rate of the Purcell filter and readout resonator which are assumed to be equal.

Furthermore, the qubit frequency and anharmonicity are determined by standard qubit spectroscopy [43].

We calibrate the photon number in the resonator n_{drive} by measuring the qubit frequency as a function of measurement drive power P_{RF} . Here, n_{drive} is assumed to be proportional to the power P_{out} transmitted through the device and measured at the FPGA, see Fig. 6(a). The proportionality factor between output power and intracavity photon number is extracted using the known χ . Due to a self-Kerr non-linearity, the output power is proportional to the input power only at low readout powers (Fig. 6(b)).

Appendix B: Preselection and histogram analysis

Preselection rejects instances in which the qubit is detected in the excited state from further analysis. Not doing so would lead to systematic errors in the experiment. Excited state detection could be due to thermal excitation, or residual excitation of the qubit from previous measurement runs. In our experiment we integrate the last 50 ns of the premeasurement pulse resulting in a mean integrated measurement value q_p to determine the state of the qubit. The histogram of these integrated values, Fig. 6(c), is fit to a Gaussian distribution (light blue line) and the state discrimination threshold (dashed vertical line) is set to the 99% of the fitted cumulative distribution function. This guarantees that the majority of thermally excited states identified by integrated measurement values larger than the threshold are rejected.

We find that the fraction of rejected events increases with resonator drive strength n_{drive} , see Fig. 6(d). This is due to measurement induced mixing which is expected to vanish for decreasing drive strength. For $n_{drive} \rightarrow 0$ we find an excess of $0.3 \pm 0.1\%$ of events rejected beyond the set threshold of 1%, which we attribute to the residual thermal population of the qubit, see Fig. 6(d). This low thermal population is a byproduct of the Purcell filter, which due to its limited bandwidth and detuning from the qubit, further reduces the effective thermal photon flux in the readout resonator at the qubit frequency. This is an additional benefit of using a Purcell filter to improve the fidelity of single-shot readout not previously discussed in Ref. [19].

For the analysis of the measurement errors as discussed in the text, the model used to fit the single-shot histograms is given by

$$\begin{bmatrix} C_g(q_\tau) \\ C_e(q_\tau) \end{bmatrix} = \begin{bmatrix} A_{gg} & A_{eg} \\ A_{ge} & A_{ee} \end{bmatrix} \begin{bmatrix} \text{PDF}[\mathcal{N}(\mu_g, \sigma_g), q_\tau] \\ \text{PDF}[\mathcal{N}(\mu_e, \sigma_e), q_\tau] \end{bmatrix}$$

where $\text{PDF}[\mathcal{N}(\mu_x, \sigma_x)]$ is a normal probability distribution function with mean and standard deviation, μ_x , σ_x and C_x are the expected counts of traces prepared in qubit state $x \in \{g, e\}$ as a function of the filtered quadrature value q_τ . A_{if} are the amplitudes with the qubit prepared in the desired state $i \in \{g, e\}$ and detected in the

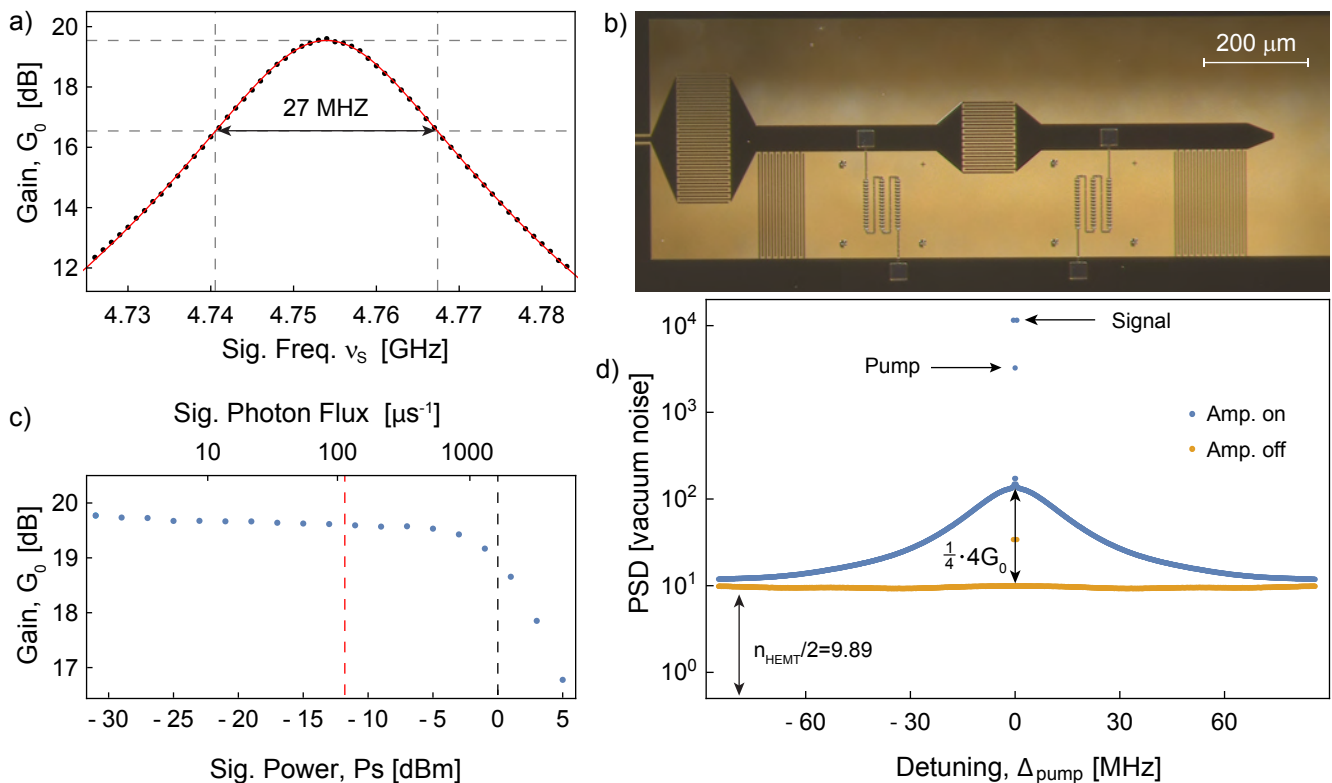


FIG. 7. a) Measurement of the gain G_0 of the amplifier versus signal frequency ν_s . The red line is a Lorentzian fit to extract the peak gain ≈ 19.7 dB and 3 dB bandwidth of 27 MHz. b) Micrograph of the Josephson Parametric Dimer used in the experiment made from etched niobium (black) on sapphire (yellow). The circuit consists of two capacitively coupled lumped element non-linear resonators each with a large finger capacitor and an array of 45 SQUIDs (shadow evaporated aluminum, gray in picture) acting as a non-linear inductor element. The left resonator is capacitively coupled to the output line of the measurement setup. c) Measurement of the gain G_0 vs. signal power P_s to extract the 1 dB compression point of the amplifier at the experimentally used bias point. The red dashed line is the optimal readout power used in the experiment while the gray dashed line depicts the 1 dB compression power. d) Power spectral density (PSD) of the amplified quadrature versus signal frequency detuning from the pump tone with the parametric amplifier on (blue) and off (yellow) used to calibrate the measurement efficiency of the output line. The y-axis is scaled such that the distance between the peak of the parametric amplifier on spectrum (blue) and the off noise spectrum (yellow) is equal to the vacuum noise times the gain, i.e. $1/4 \cdot 4G_0$.

final state $f \in \{g, e\}$. This model does not accurately account for transitions that occur during the measurement but only for ones that occurred between state preparation and the beginning of the measurement. For the short measurement times considered here this is a reasonably good approximation.

Appendix C: Calibration of measurement efficiency

We perform power spectral density measurements of the noise added by the amplifiers in the output line to calibrate the measurement efficiency $\eta = \eta_{\phi\text{amp}}\eta_{\text{loss}}$ of our output line characterized by the parametric amplifier's noise performance $\eta_{\phi\text{amp}}$ and the loss before the amplifier η_{loss} . We achieve parametric gain by pumping the amplifier [28] with a coherent tone at the readout frequency. The maximum gain is adjusted by varying the pump power and the flux bias through the su-

perconducting quantum interference device (SQUID) arrays. The pump tone is interferometrically canceled by adjusting the phase and amplitude of a cancellation tone coupled via the directional coupler to the output of the JPD. This minimizes pump leakage back toward the sample and avoids saturation of following amplifiers along the output line. The frequency dependent gain peaks at $G_0 = 19.7$ dB, see Figure 7(a), at the desired signal frequency of 4.754 GHz used in the experiment. By sweeping the signal power we determine the 1 dB compression point of the amplifier (Fig. 7(c)), which is about 10 dB higher than the power used for measuring the qubit state in our experiment.

Next, we characterize the amplifier's measurement efficiency when operating in the phase-sensitive mode $\eta_{\phi\text{amp}}$, i.e. amplifying and detecting only one quadrature of the signal field. In order to create a single quadrature signal distinguishable from the pump we apply two coherent signals of equal power and opposite detuning from the pump tone. We then adjust the phase of the two

tones so that the resulting signal is oriented along the amplified quadrature, achieving a phase sensitive gain, $4G_0$. For this measurement, the ADC samples the output signal for $8.192 \mu\text{s}$ with 1 ns resolution, resulting in a frequency resolution of approximately 112 kHz. We therefore chose to detune the signals 488 kHz above and below the pump, which is an integer multiple of this resolution. Finally, we measure the noise performance of the amplified quadrature by measuring its power spectral density (PSD). The down conversion local oscillator phase is also adjusted to maximize the gain along the real quadrature of the complex signal entering the ADC as is done for the main experiment. We use the FPGA to take the real component of the complex signal and compute the auto-correlation function and average the results over a million times. The Fourier transform of this data then reveals the noise spectral density of this quadrature as seen in Figure 7(d). When the JPD is on, the overall noise level increases compared to when it is off following the frequency dependent gain of the amplifier. The two coherent signal peaks can be easily distinguished from the noise floor in both the amplifier on and off spectra, as well as the pump tone for the amplifier on case.

With the assumption that the noise of the parametric amplifier is dominated by amplified vacuum noise, the spectral density measurements are scaled so that the noise increase when turning on the JPD is equal to $4G_0 \cdot 1/4$. In this expression, $1/4$ represents the noise at the input of the parametric amplifier in the amplified quadrature and $4G_0$ is the gain of this quadrature. The resulting noise offset, $n_{\text{HEMT}}/2$ is 9.89 times larger than the vacuum level. This offset is predominately due to the noise added by the following HEMT amplifier at the 4 K temperature stage and is divided by 2 to account for the single quadrature measurement. Following Frii's formula for noise performance of cascaded amplifier chains [44], this added noise will be divided by the gain of the parametric amplifier resulting in $\eta_{\phi\text{amp}} = (1 + n_{\text{HEMT}}/(2G_0))^{-1}$. We estimate that with a gain of $4G_0 = 26 \text{ dB}$, the noise performance is about $\eta_{\phi\text{amp}} = 0.92$. If we adjust the pump settings to increase the gain to $4G_0 = 35 \text{ dB}$, at the cost of bandwidth, we find the amplifier can achieve $\eta_{\phi\text{amp}} = 0.99$.

Finally, we determine the transmission efficiency η_{loss} between the output of the sample and the input of the parametric amplifier by comparing the coherent signal power in the scaled PSD measurement to the expected power calibrated with the AC stark shift measurement, i.e. $P_{\text{out}} = (\chi/J)^2 \kappa_p n_{\text{drive}}$. The $(\chi/J)^2$ prefactor is a result of driving the circuit through the input of the Purcell filter and not the readout resonator directly [27]. The ratio between the scaled PSD measurement signal power and P_{out} is equal to the transmission efficiency and found to be $\eta_{\text{loss}} \approx 0.75$ corresponding to approximately 1.3 dB attenuation. This is well within the specified insertion loss of the elements between the sample and amplifier. The measured total efficiency of the line is determined to be $\eta = \eta_{\text{loss}}\eta_{\phi\text{amp}} = 0.66$ for 26 dB gain and $\eta = 0.75$ for 35 dB gain.

Appendix D: Overlap error model

We model the readout as a measurement of a random variable from the qubit state Gaussian distributions which have opposite means $\pm S(t)/2$ (see SecIII) and equal variance, $\sigma^2(t) = 1/(4\eta)$ at time t . With no state transitions, the optimal threshold is at the intersection of the two distributions and including both analog and digital filtering we find

$$\epsilon_o(\tau) = \text{erfc} \left[\sqrt{\frac{1}{8} \frac{\int_0^\tau S(t) f(\tau-t) dt}{\int_0^\tau \sigma^2(t) f(\tau-t) dt}} \right] \quad (\text{D1})$$

where $f(\tau-t)$ is the response function of the relevant filter elements for the measurement of s_τ . In our experiment, $f(\tau-t)$ consists of the narrow bandwidth parametric amplifier, the 8 ns box car integration of the FPGA and the mode-matched digital weighting function $W(t)$. We use this model along with the numerical solutions of $S(t)$ using the full system equations (no quasi-steady state assumption [27]), to determine the theory curves (green) in Fig. 3(a-b) of the main text.

-
- [1] D. P. DiVincenzo, Phys. Scr. **2009**, 014020 (2009).
 [2] R. Barends, J. Kelly, A. Megrant, A. Veitia, D. Sank, E. Jeffrey, T. C. White, J. Mutus, A. G. Fowler, B. Campbell, Y. Chen, Z. Chen, B. Chiaro, A. Dunsworth, C. Neill, P. O'Malley, P. J. J., P. Roushan, A. Vainsencher, J. Wenner, A. N. Korotkov, A. N. Cleland, and J. M. Martinis, Nature **508**, 500 (2014).
 [3] C. H. Bennett, G. Brassard, C. Crépeau, R. Jozsa, A. Peres, and W. K. Wootters, Phys. Rev. Lett. **70**, 1895 (1993).
 [4] L. Steffen, Y. Salathe, M. Oppliger, P. Kurpiers, M. Baur, C. Lang, C. Eichler, G. Puebla-Hellmann, A. Fedorov, and A. Wallraff, Nature **500**, 319 (2013).
 [5] J. E. Johnson, C. Macklin, D. H. Slichter, R. Vijay, E. B. Weingarten, J. Clarke, and I. Siddiqi, Phys. Rev. Lett. **109**, 050506 (2012).
 [6] D. Ristè, J. G. van Leeuwen, H.-S. Ku, K. W. Lehnert, and L. DiCarlo, Phys. Rev. Lett. **109**, 050507 (2012).
 [7] J. F. Clauser, M. A. Horne, A. Shimony, and R. A. Holt, Phys. Rev. Lett. **23**, 880 (1969).
 [8] M. Ansmann, H. Wang, R. C. Bialczak, M. Hofheinz, E. Lucero, M. Neeley, A. D. O'Connell, D. Sank, M. Weides, J. Wenner, A. N. Cleland, and J. M. Martinis, Nature **461**, 504 (2009).

- [9] B. Hensen, H. Bernien, A. E. Dreau, A. Reiserer, N. Kalb, M. S. Blok, J. Ruitenberg, R. F. L. Vermeulen, R. N. Schouten, C. Abellan, W. Amaya, V. Pruneri, M. W. Mitchell, M. Markham, D. J. Twitchen, D. Elkouss, S. Wehner, T. H. Taminiou, and R. Hanson, *Nature* **526**, 682 (2015).
- [10] A. Blais, R.-S. Huang, A. Wallraff, S. M. Girvin, and R. J. Schoelkopf, *Phys. Rev. A* **69**, 062320 (2004).
- [11] A. Wallraff, D. I. Schuster, A. Blais, L. Frunzio, J. Majer, S. M. Girvin, and R. J. Schoelkopf, *Phys. Rev. Lett.* **95**, 060501 (2005).
- [12] C. M. Caves, *Phys. Rev. D* **26**, 1817 (1982).
- [13] B. Yurke, M. L. Roukes, R. Movshovich, and A. N. Pargellis, *Appl. Phys. Lett.* **69**, 3078 (1996).
- [14] M. A. Castellanos-Beltran, K. D. Irwin, G. C. Hilton, L. R. Vale, and K. W. Lehnert, *Nat. Phys.* **4**, 929 (2008).
- [15] A. A. Clerk, M. H. Devoret, S. M. Girvin, F. Marquardt, and R. J. Schoelkopf, *Rev. Mod. Phys.* **82**, 1155 (2010).
- [16] F. Mallet, F. R. Ong, A. Palacios-Laloy, F. Nguyen, P. Bertet, D. Vion, and D. Esteve, *Nat. Phys.* **5**, 791 (2009).
- [17] R. Vijay, D. H. Slichter, and I. Siddiqi, *Phys. Rev. Lett.* **106**, 110502 (2011).
- [18] M. D. Reed, B. R. Johnson, A. A. Houck, L. DiCarlo, J. M. Chow, D. I. Schuster, L. Frunzio, and R. J. Schoelkopf, *Appl. Phys. Lett.* **96**, 203110 (2010).
- [19] E. Jeffrey, D. Sank, J. Y. Mutus, T. C. White, J. Kelly, R. Barends, Y. Chen, Z. Chen, B. Chiaro, A. Dunsworth, A. Megrant, P. J. J. O'Malley, C. Neill, P. Roushan, A. Vainsencher, J. Wenner, A. N. Cleland, and J. M. Martinis, *Phys. Rev. Lett.* **112**, 190504 (2014).
- [20] N. T. Bronn, Y. Liu, J. B. Hertzberg, A. D. Córcoles, A. A. Houck, J. M. Gambetta, and J. M. Chow, *Applied Physics Letters* **107**, 172601 (2015).
- [21] J. Y. Mutus, T. C. White, R. Barends, Y. Chen, Z. Chen, B. Chiaro, A. Dunsworth, E. Jeffrey, J. Kelly, A. Megrant, C. Neill, P. J. J. O'Malley, P. Roushan, D. Sank, A. Vainsencher, J. Wenner, K. M. Sundqvist, A. N. Cleland, and J. M. Martinis, *Applied Physics Letters* **104**, 263513 (2014).
- [22] C. Macklin, K. O'Brien, D. Hover, M. E. Schwartz, V. Bolkhovskiy, X. Zhang, W. D. Oliver, and I. Siddiqi, *Science* **350**, 307 (2015).
- [23] T. Roy, S. Kundu, M. Chand, A. M. Vadiraj, A. Ranadive, N. Nehra, M. P. Patankar, J. Aumentado, A. A. Clerk, and R. Vijay, *Applied Physics Letters* **107**, 262601 (2015).
- [24] P. Krantz, A. Bengtsson, M. Simoen, S. Gustavsson, V. Shumeiko, W. D. Oliver, C. M. Wilson, P. Delsing, and J. Bylander, *Nat Commun* **7**, (2016).
- [25] Y. Liu, S. J. Srinivasan, D. Hover, S. Zhu, R. McDermott, and A. A. Houck, *New Journal of Physics* **16**, 113008 (2014).
- [26] D. T. McClure, H. Paik, L. S. Bishop, M. Steffen, J. M. Chow, and J. M. Gambetta, *Phys. Rev. Applied* **5**, 011001 (2016).
- [27] E. A. Sete, J. M. Martinis, and A. N. Korotkov, *Phys. Rev. A* **92**, 012325 (2015).
- [28] C. Eichler, Y. Salathe, J. Mlynek, S. Schmidt, and A. Wallraff, *Phys. Rev. Lett.* **113**, 110502 (2014).
- [29] F. Motzoi, J. M. Gambetta, P. Rebentrost, and F. K. Wilhelm, *Phys. Rev. Lett.* **103**, 110501 (2009).
- [30] J. M. Gambetta, F. Motzoi, S. T. Merkel, and F. K. Wilhelm, *Phys. Rev. A* **83**, 012308 (2011).
- [31] J. Gambetta, W. A. Braff, A. Wallraff, S. M. Girvin, and R. J. Schoelkopf, *Phys. Rev. A* **76**, 012325 (2007).
- [32] C. C. Bultink, M. A. Rol, T. E. O'Brien, X. Fu, B. C. S. Dikken, C. Dickel, R. F. L. Vermeulen, J. C. de Sterke, A. Bruno, R. N. Schouten, and L. DiCarlo, *Phys. Rev. Applied* **6**, 034008 (2016).
- [33] J. Gambetta, A. Blais, D. I. Schuster, A. Wallraff, L. Frunzio, J. Majer, M. H. Devoret, S. M. Girvin, and R. J. Schoelkopf, *Phys. Rev. A* **74**, 042318 (2006).
- [34] J. Koch, T. M. Yu, J. Gambetta, A. A. Houck, D. I. Schuster, J. Majer, A. Blais, M. H. Devoret, S. M. Girvin, and R. J. Schoelkopf, *Phys. Rev. A* **76**, 042319 (2007).
- [35] J. Schreier, A. Houck, J. Koch, D. I. Schuster, B. Johnson, J. Chow, J. Gambetta, J. Majer, L. Frunzio, M. Devoret, S. Girvin, and R. Schoelkopf, *Phys. Rev. B* **77**, 180502 (2008).
- [36] M. Khezri, E. Mlinar, J. Dressel, and A. N. Korotkov, *Phys. Rev. A* **94**, 012347 (2016).
- [37] M. Boissonneault, J. M. Gambetta, and A. Blais, *Phys. Rev. Lett.* **105**, 100504 (2010).
- [38] D. Sank, Z. Chen, M. Khezri, J. Kelly, R. Barends, B. Campbell, Y. Chen, B. Chiaro, A. Dunsworth, A. Fowler, and et al., *Physical Review Letters* **117**, 190503 (2016).
- [39] M. Boissonneault, J. M. Gambetta, and A. Blais, *Phys. Rev. A* **79**, 013819 (2009).
- [40] D. H. Slichter, R. Vijay, S. J. Weber, S. Boutin, M. Boissonneault, J. M. Gambetta, A. Blais, and I. Siddiqi, *Phys. Rev. Lett.* **109**, 153601 (2012).
- [41] Y. Chen, D. Sank, P. O'Malley, T. White, R. Barends, B. Chiaro, J. Kelly, E. Lucero, M. Mariantoni, A. Megrant, C. Neill, A. Vainsencher, J. Wenner, Y. Yin, A. N. Cleland, and J. M. Martinis, *Applied Physics Letters* **101**, 182601 (2012).
- [42] A. A. Houck, J. A. Schreier, B. R. Johnson, J. M. Chow, J. Koch, J. M. Gambetta, D. I. Schuster, L. Frunzio, M. H. Devoret, S. M. Girvin, and R. J. Schoelkopf, *Phys. Rev. Lett.* **101**, 080502 (2008).
- [43] D. I. Schuster, A. Wallraff, A. Blais, L. Frunzio, R.-S. Huang, J. Majer, S. M. Girvin, and R. J. Schoelkopf, *Phys. Rev. Lett.* **94**, 123602 (2005).
- [44] D. M. Pozar, *Microwave engineering* (Wiley & Sons, Hoboken, 2012).